



Phenomenological modeling for magneto-mechanical couplings of martensitic variant reorientation in ferromagnetic shape memory alloys

Yuxiang Han¹ · Linxiang Wang¹ · Roderick Melnik²

Received: 12 August 2022 / Accepted: 27 October 2022 / Published online: 14 November 2022
© The Author(s), under exclusive licence to Springer-Verlag GmbH, DE part of Springer Nature 2022

Abstract

The paper presents a 2D phenomenological model to characterize the magneto-mechanical coupled behavior and its temperature dependences for martensitic variant reorientation in ferromagnetic shape memory alloys. A set of state variables are chosen to describe different microscopic mechanisms, and the evolution rules for the state variables are determined by minimizing the thermodynamic potential. The modified Landau free energy function is employed to account for the hysteretic switching between martensitic variants. It is assumed that the local switching thresholds are distributed due to the non-uniform internal stress throughout the specimen. The governing equation for martensite reorientation is then homogenized by taking this distribution property into account. The concept of density reassignment is also deployed to improve the modeling accuracy for partial reorientations. To validate the model capability, the model formulation is numerically implemented for the typical loading condition (i.e., uniaxial stress and a perpendicular magnetic field). As one of the superiorities, the temperature-dependent properties are remarked for the proposed model as well. Comparisons between the model predictions and the experimental results demonstrate the model capability in addressing the magneto-mechanical couplings and the temperature dependences of martensite reorientation.

Keywords Ferromagnetic shape memory alloy · Martensitic variant reorientations · Phenomenological model · Hysteretic switching · Magneto-mechanical couplings

1 Introduction

Ferromagnetic shape memory alloys (FSMAs), as an emerging kind of smart materials, have been intensively studied in the past two decades, since they were first reported in 1996 [1, 2]. Ni–Mn–Ga single crystals are the most widely investigated FSMAs, and the tetragonal martensite is commonly observed. Accompanied by magnetization changes, the giant magnetic field-induced strain was detected [3, 4], which is one or two orders of magnitude higher than in traditional magnetostrictive materials. FSMAs are also known for their relatively low blocking stress and high operating

frequencies. It is generally believed that the unique magneto-mechanical behavior results from three microscopic mechanisms, i.e., magnetic domain wall motion, rotation of magnetization vectors, and martensitic variant reorientation [5].

In literature, theoretical models have been proposed to study the magneto-mechanical couplings in FSMAs and these models can be mainly classified as simple-energy models, phase-field models and phenomenological models. Models with simple-energy relations were first developed to investigate the magneto-mechanical coupled behaviors [4, 6–8]. Even though simple-energy relations can qualitatively explain the stress dependences on the field-induced strains, these early models seem to be incompetent to tackle the hysteretic nonlinearity of material responses. Phase-field simulations have been conducted to investigate the microstructural evolution with sophisticated energy formulation [9–12]. Based on Landau’s theory, phase-field modeling provides a flexible framework with a set of partial differential equations, which always requires intensive computational cost. In practice, computational inefficiency makes

✉ Linxiang Wang
wanglx236@zju.edu.cn

¹ State Key Laboratory of Fluid Power and Mechatronic Systems, Zhejiang University, Hangzhou 310027, China

² MS2Discovery Interdisciplinary Research Institute, Wilfrid Laurier University, Waterloo, ON N2L 3L5, Canada

phase-field models unsuitable for the engineering applications of FSMA elements. It is worth noting that most existing models for FSMA are the phenomenological models that are proposed to quantitatively predict the macroscopic strain and magnetization responses. Many of phenomenological models are developed within the thermodynamic framework of irreversible processes, in which the martensite reorientation is characterized by plastic hardening. Kiefer and Lagoudas [13] presented a thermodynamic phenomenological model to investigate the reorientation between two variants, in which the evolution of internal state variables is associated with the macroscopic coupled responses. Even though the evolution of internal state variables effectively characterizes three microscopic mechanisms, the modeling accuracy still hinders the utility of phenomenological models. In the last decade, some modifications were presented to improve the capability of models in this field [14–17]. 3D constitutive theories were also proposed in recent years to describe the material responses under 3D complex loadings [18–22]. In practice, it is challenging to realize 3D coupled loadings in many engineering applications. Therefore, most thermodynamic models only consider the coexistence of two tetragonal variants under 2D magneto-mechanical loadings for the sake of simplicity. Besides, most macroscopic models concentrate on the magneto-mechanical couplings, but the temperature-dependent behaviors are less emphasized. Several experiments [23–30] have been conducted to study the temperature dependences of the martensite reorientation, revealing that the material temperature remarkably affects the strain and magnetization responses. Therefore, it is necessary to simulate the temperature dependences of the martensite reorientation under magneto-mechanical loadings.

Motivated by this and aiming at facilitating the design and control of FSMA-based smart structures, a phenomenological model is presented here to capture the magneto-mechanical coupling characteristics and predict the temperature-dependent properties of the macroscale material responses. The major contributions of this paper can be summarized by the following three aspects. Firstly, a set of state variables are chosen to account for all three microscopic mechanisms and the evolution laws for state variables are found from the minimum energy principle. The Gibbs free energy function is employed as the thermodynamic potential. Apart from the mechanical and magnetic parts, a modified Landau free energy function is encompassed in the energy formulation as well. Instead of plastic hardening, the martensite reorientation is simulated as hysteretic switching between stable equilibria. Inspired by the traditional Landau theory for phase transitions, the modified Landau free energy function is defined by piecewise quadratic polynomials, whose minima indicate the stable equilibria of material configuration. The local hysteretic switching of martensitic variants is characterized by the switching between these minima.

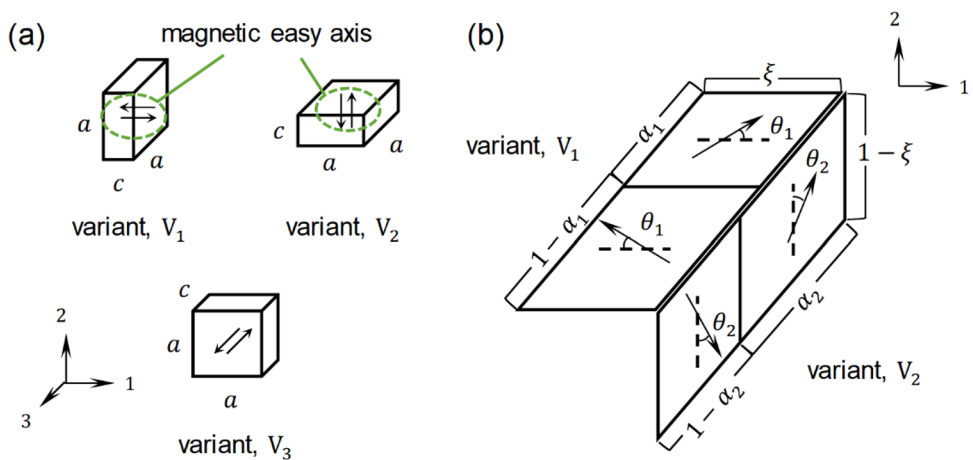
Secondly, the evolution rule for martensite reorientation is homogenized to upgrade the model adaptability and the concept of density reassignment [31] is developed to improve the modeling accuracy for partial reorientations. It is presumed that the local switching thresholds follow a certain distribution property due to the distributed internal stress. To compensate for the drawback of sudden switching, the evolution rule for martensite reorientation is homogenized by taking the distributed local switching thresholds into account, which is formulated as the weighted sum of local switching responses. Based on the assumption of distributed local thresholds, the strategy of density reassignment provides a straightforward way to approximate the reversal curves for partial reorientations, which utilizes the self-similarity between the outer evolution branches and the inner reversal curves. The strategy enables one to directly predict the reversal curves from the hysteresis loop for complete reorientations, which not only improves the prediction accuracy but also saves the computational cost. Thirdly, the temperature dependences of martensite reorientation are addressed in the proposed model. For one thing, some material constants vary with the material temperature, and their temperature dependences are determined by curve fitting. For another, the local switching thresholds are assumed to count on the material temperature, resulting in the temperature-dependent distribution properties. By combining these factors, the proposed model can qualitatively capture the trends of temperature-dependent material responses, which improves the model adaptability.

The remainder of this paper is organized as follows. The model formulation is developed in Sect. 2, in which the evolution rules of state variables are derived under 2D magneto-mechanical loadings. In Sect. 3, the local switching pattern is formulated and then extended to obtain the upgraded evolution rule for martensite reorientation, and the idea of density reassignment is developed to facilitate the prediction of incomplete reorientations. The details of model validation are presented in Sect. 4, and the temperature dependences are discussed for the proposed model as well. Comparisons between the model predictions and the experimental data are given in Sect. 5 while concluding remarks are provided in Sect. 6.

2 Model formulation

In the current section, the model formulation is developed to investigate the martensitic variant reorientation and determine the macroscopic material responses under 2D magneto-mechanical loadings. The material temperature is assumed to be uniform throughout the specimen and the heat transfer is not involved in the proposed model. The state variables are chosen to characterize three microscopic mechanisms

Fig. 1 The schematic representation for **a** the crystal structure of tetragonal martensitic variants in Ni–Mn–Ga single crystals, and **b** the coexistence of martensitic variants and magnetic domains as well as the rotation of magnetization vectors



under the coupled loadings, and the evolution rules for these state variables are phenomenologically obtained from the minimum energy principle.

2.1 Choice of state variables

Figure 1a depicts the crystal structure of martensite in Ni–Mn–Ga single crystals, where the tetragonal martensitic variants are considered for convenience. The tetragonal unit cell has short and long edges of length c and a respectively, and three martensitic variants, i.e., V_1 , V_2 and V_3 , are named after the direction of their short edges. Besides, the martensitic variants are spontaneously magnetized and the magnetic easy axes are aligned with their short edges. As mentioned above, the current model is employed to predict the material responses under 2D external loadings. It is assumed that no external loads are applied in the third direction and the coexistence of only two variants, i.e., V_1 and V_2 , are considered in the rest of the paper. As is widely accepted, the magneto-mechanical couplings are attributed to three microscopic mechanisms, namely magnetic domain wall motion, rotation of magnetization vectors, and martensitic variant reorientation. Figure 1b is employed to illustrate the idealized coexistence of V_1 and V_2 , the independent magnetic domains and the rotation of magnetization vectors [15]. The volume fractions of V_1 and V_2 are given by ξ and $1 - \xi$, respectively. α_i and θ_i denote the volume fractions of magnetic domains and the rotation angles of local magnetization vectors away from the magnetic easy axes in the variants V_i (for $i = 1, 2$). Based on the schematic representation shown in Fig. 1b, ξ , α_i and θ_i are chosen as the state variables to account for the microscopic mechanisms. Moreover, it should be noted that the constraints, $0 \leq \xi \leq 1$, $0 \leq \alpha_i \leq 1$

and $-\pi/2 \leq \theta_i \leq \pi/2$, need to be satisfied for these state variables. When the specimen is subjected to magneto-mechanical loadings, i.e. magnetic field \mathbf{H} and stress $\boldsymbol{\sigma}$, the macroscopic responses can be simply derived from the evolution of these state variables. On the one hand, the internal magnetization vector \mathbf{M} is defined in a weighted average sense, given by

$$\mathbf{M} = M_s \begin{bmatrix} \xi(2\alpha_1 - 1)\cos\theta_1 + (1 - \xi)\sin\theta_2 \\ \xi\sin\theta_1 + (1 - \xi)(2\alpha_2 - 1)\cos\theta_2 \\ 0 \end{bmatrix}, \quad (1)$$

where M_s denotes the saturation magnetization. In particular, $\alpha_1 = \alpha_2 = 1/2$ and $\theta_1 = \theta_2 = 0$ hold when no external field is applied, implying that no magnetization output is detected under zero field. On the other hand, the strain tensor $\boldsymbol{\epsilon}$ is decomposed into the elastic part and the inelastic part as

$$\boldsymbol{\epsilon} = \boldsymbol{\epsilon}_{\text{el}} + \boldsymbol{\epsilon}_{\text{in}} \quad (2)$$

The first term $\boldsymbol{\epsilon}_{\text{el}}$ denotes the strain due to elastic deformation, which is given by

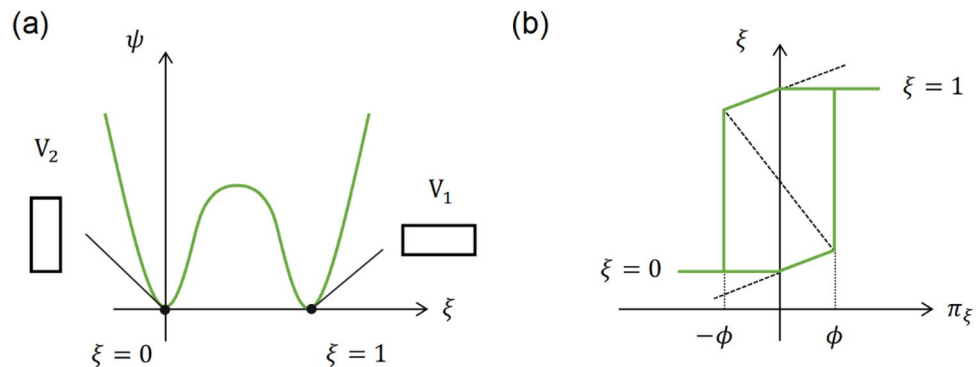
$$\boldsymbol{\epsilon}_{\text{el}} = \xi \mathbf{S}_1 : \boldsymbol{\sigma} + (1 - \xi) \mathbf{S}_2 : \boldsymbol{\sigma}, \quad (3)$$

where \mathbf{S}_1 and \mathbf{S}_2 are the compliance tensors for V_1 and V_2 , respectively. The second term $\boldsymbol{\epsilon}_{\text{in}}$ denotes the inelastic strain due to martensite reorientation, given by

$$\boldsymbol{\epsilon}_{\text{in}} = -\epsilon_r \begin{bmatrix} \xi & 0 & 0 \\ 0 & 1 - \xi & 0 \\ 0 & 0 & 0 \end{bmatrix}, \quad (4)$$

where ϵ_r refers to the maximum reorientation strain. The value of ϵ_r can be either calibrated from the field-free uniaxial compression test, or approximated from the tetragonality of the martensite unit cell, i.e., $\epsilon_r \approx 1 - c/a$.

Fig. 2 The plots of **a** the modified Landau free energy function, and **b** the hysteretic switching between the stable equilibria $\xi = 0$ and $\xi = 1$



2.2 Evolution rules for state variables

The Gibbs free energy function G is employed as the thermodynamic potential, which involves the mechanical part G^{mec} , the magnetic part G^{mag} and the modified Landau free energy function ψ . In other words, the energy formulation is given by

$$G = G^{\text{mec}} + G^{\text{mag}} + \psi \quad (5)$$

The mechanical potential is the energy contribution due to mechanical deformation, having the form

$$G^{\text{mec}} = -\frac{1}{2}\boldsymbol{\sigma} : (\xi S_1 + (1 - \xi)S_2) : \boldsymbol{\sigma} - \boldsymbol{\sigma} : \boldsymbol{\epsilon}_{\text{in}}, \quad (6)$$

in which the first term is the elastic strain energy while the second term denotes the mechanical work done by the inelastic reorientation. The magnetic potential is given by

$$G^{\text{mag}} = K_u(\xi \sin^2 \theta_1 + (1 - \xi) \sin^2 \theta_2) - \mu_0 \mathbf{M} \cdot \mathbf{H} - \frac{1}{2} \mu_0 \mathbf{M} \cdot \mathbf{H}_d \quad (7)$$

The first term above is the magnetocrystalline anisotropy energy where K_u is the anisotropy constant. The magnetocrystalline anisotropy energy is expressed as the weighted sum of contributions from V_1 and V_2 , reflecting the work done by rotating the internal magnetization vectors. The second term in Eq. (7) denotes the Zeeman energy that accounts for the interaction between the internal magnetization and the external magnetic field, while $\mu_0 = 4\pi \times 10^{-7} \text{ T} \cdot \text{m} \cdot \text{A}^{-1}$ is the vacuum permeability. The last term refers to the magnetostatic energy [32] which is associated with the demagnetization effect inside the specimen, where \mathbf{H}_d is the internal demagnetizing field. The demagnetizing field is not uniform inside the specimen but its average value can be approximated from the internal magnetization using the relation

$$\mathbf{H}_d = -D\mathbf{M}, \quad (8)$$

where $D = \text{diag}(D_1, D_2, D_3)$ is the demagnetizing tensor with a trace of one. It should be noted that the demagnetizing tensor depends on the sample geometry and Eq. (8) only works for ellipsoids. Nonetheless, it has been demonstrated to be sufficiently accurate for rectangular prisms [14, 15, 17]. The modified Landau free energy function $\psi(\xi)$ is employed to characterize the hysteretic behavior in martensite reorientation and the volume fraction ξ is exploited as the order parameter. Herein, the modified Landau free energy function is defined as C^1 -continuous piecewise quadratic polynomials, given by

$$\psi(\xi) = \begin{cases} \frac{\kappa_1}{2}\xi^2, & \text{if } \kappa_1\xi < \phi \\ \frac{\kappa_1}{2}(1 - \xi)^2, & \text{if } \kappa_1(1 - \xi) < \phi \\ \frac{\kappa_2}{2}\left(\frac{1}{2} - \xi\right)^2 + \Delta\psi, & \text{otherwise} \end{cases} \quad (9)$$

where κ_1 , κ_2 , ϕ , and $\Delta\psi$ are positive coefficients. Enforcing the continuity further gives $\kappa_2 = 2\kappa_1\phi/(2\phi - \kappa_1)$ and $\Delta\psi = \phi/4$. Figure 2a provides the plot of the modified Landau free energy function that achieves its local minima at $\xi = 0$ and $\xi = 1$. These local minima correlate with the stable equilibria that the material is fully occupied by V_2 and V_1 , respectively. The switching between these minima is regarded as the reorientation between two variants. It is worth noting that the double-well potential is used to manifest the relative stability between different equilibria, which effectively captures the hysteresis behavior in martensitic variant reorientation.

As mentioned earlier, the evolution of the state variables is determined by minimizing the thermodynamic potential, implying that

$$\frac{\partial G}{\partial \alpha_i} = 0, \frac{\partial G}{\partial \theta_i} = 0 \text{ and } \frac{\partial G}{\partial \xi} = 0 \quad (10)$$

Substituting the energy formulation into Eq. (10) gives the governing equations for these state variables, and the strain and magnetization responses can be updated by numerically solving these governing equations. Specifically, the governing equations for magnetic domain wall motion are given by

$$\xi(2\alpha_1 - 1)\cos\theta_1 + (1 - \xi)\sin\theta_2 = \frac{H_1}{D_1 M_s}, \quad (11)$$

and

$$\xi\sin\theta_1 + (1 - \xi)(2\alpha_2 - 1)\cos\theta_2 = \frac{H_2}{D_2 M_s} \quad (12)$$

The governing equations for the rotation of magnetization vectors are given by

$$\begin{aligned} & 2K_u \sin\theta_1 \cos\theta_1 - \mu_0 D_1 M_s^2 (2\alpha_1 - 1) \sin\theta_1 \\ & \left(\xi(2\alpha_1 - 1) \cos\theta_1 + (1 - \xi)\sin\theta_2 - \frac{H_1}{D_1 M_s} \right) \\ & + \mu_0 D_2 M_s^2 \cos\theta_1 \left(\xi\sin\theta_1 + (1 - \xi)(2\alpha_2 - 1)\cos\theta_2 - \frac{H_2}{D_2 M_s} \right) = 0, \end{aligned} \quad (13)$$

and

$$\begin{aligned} & 2K_u \sin\theta_2 \cos\theta_2 + \mu_0 D_1 M_s^2 \cos\theta_2 \left(\xi(2\alpha_1 - 1) \cos\theta_1 + (1 - \xi)\sin\theta_2 - \frac{H_1}{D_1 M_s} \right) \\ & - \mu_0 D_2 M_s^2 (2\alpha_2 - 1) \sin\theta_2 \left(\xi\sin\theta_1 + (1 - \xi)(2\alpha_2 - 1)\cos\theta_2 - \frac{H_2}{D_2 M_s} \right) = 0, \end{aligned} \quad (14)$$

Finally, the governing equation for martensitic variant reorientation is given by

$$\begin{aligned} & \frac{\partial\psi}{\partial\xi} - \frac{1}{2}\boldsymbol{\sigma} : (\mathbf{S}_1 - \mathbf{S}_2) : \boldsymbol{\sigma} - \boldsymbol{\sigma} : \frac{\partial\epsilon_{in}}{\partial\xi} + K_u(\sin^2\theta_1 - \sin^2\theta_2) + \\ & \mu_0 D_1 M_s^2 ((2\alpha_1 - 1)\cos\theta_1 - \sin\theta_2) \left(\xi(2\alpha_1 - 1)\cos\theta_1 + (1 - \xi)\sin\theta_2 - \frac{H_1}{D_1 M_s} \right) + \\ & \mu_0 D_2 M_s^2 (\sin\theta_1 - (2\alpha_2 - 1)\cos\theta_2) \left(\xi\sin\theta_1 + (1 - \xi)(2\alpha_2 - 1)\cos\theta_2 - \frac{H_2}{D_2 M_s} \right) = 0, \end{aligned} \quad (15)$$

where the term $\frac{\partial\psi}{\partial\xi}$ can be obtained by differentiating Eq. (9) with respect to ξ .

3 Model extensions

Martensitic variant reorientation features substantial hysteresis and nonlinearities, which is regarded as an irreversible process. In the previous subsection, the modified Landau free energy function has been utilized to

characterize the switching between martensitic variants. The hysteretic evolution of ξ can be simply demonstrated if one rewrites Eq. (15) as

$$\frac{\partial\psi}{\partial\xi} = \pi_\xi(\boldsymbol{\sigma}, \mathbf{H}, \alpha_i, \theta_i, \xi), \quad (16)$$

where π_ξ denotes the generalized force that drives the martensite reorientation. The force π_ξ is a function of external loads and state variables, given by

$$\begin{aligned} \pi_\xi(\boldsymbol{\sigma}, \mathbf{H}, \alpha_i, \theta_i, \xi) = & \frac{1}{2}\boldsymbol{\sigma} : (\mathbf{S}_1 - \mathbf{S}_2) : \boldsymbol{\sigma} + \boldsymbol{\sigma} : \frac{\partial\epsilon_{in}}{\partial\xi} - K_u(\sin^2\theta_1 - \sin^2\theta_2) - \\ & \mu_0 D_1 M_s^2 ((2\alpha_1 - 1)\cos\theta_1 - \sin\theta_2) \left(\xi(2\alpha_1 - 1)\cos\theta_1 + (1 - \xi)\sin\theta_2 - \frac{H_1}{D_1 M_s} \right) - \\ & \mu_0 D_2 M_s^2 (\sin\theta_1 - (2\alpha_2 - 1)\cos\theta_2) \left(\xi\sin\theta_1 + (1 - \xi)(2\alpha_2 - 1)\cos\theta_2 - \frac{H_2}{D_2 M_s} \right) \end{aligned} \quad (17)$$

It should be noted that the hysteresis in the evolution of ξ results from the non-convexity of the modified Landau free energy function. Figure 2b illustrates the hysteretic switching between $\xi = 0$ and $\xi = 1$, which delineates the irreversible reorientation between V_2 and V_1 . It can be seen that V_2 becomes unstable and reorients to V_1 when π_ξ increases to ϕ ,

while V_1 loses its stability and jumps to V_2 when π_ξ decreases to $-\phi$. The coefficient ϕ in Eq. (9) can be deemed as the driving

force required for martensite reorientation, and two equilibrium states switch to each other when the force π_ξ reaches the switching thresholds ϕ or $-\phi$. In other words, the evolution rule for ξ is simply given by

$$\xi = \begin{cases} L_\phi^+[\pi_\xi], & \text{for } \dot{\xi} > 0 \\ L_\phi^-[\pi_\xi], & \text{for } \dot{\xi} < 0 \end{cases}, \quad (18)$$

where the notations $L_\phi^+[\cdot]$ and $L_\phi^-[\cdot]$ describe the sudden switching between $\xi = 0$ and $\xi = 1$. The definitions of $L_\phi^+[\cdot]$ and $L_\phi^-[\cdot]$ are given by

$$L_\phi^+[u] = \begin{cases} 0, & \text{if } u \leq 0 \\ \frac{u}{\kappa_1}, & \text{if } 0 < u < \phi \\ 1, & \text{otherwise} \end{cases} \quad (19)$$

and

$$L_\phi^-[u] = \begin{cases} 1, & \text{if } u \leq -\phi \\ 1 - \frac{u}{\kappa_1}, & \text{if } -\phi < u < 0 \\ 0, & \text{otherwise} \end{cases} \quad (20)$$

Even if Eqs. (19) and (20) effectively capture the hysteretic switching between variants, such a switching pattern is still insufficient to simulate the martensite reorientation. The sudden switching between the equilibria disables ξ to evolve in a smooth and gradual manner, which is observed in the magneto-mechanical tests of single-crystal bulks. Therefore, some improvements must be made to compensate for the drawbacks and thereby upgrade the model adaptability. In the current model, it is assumed that the gradual reorientation of martensitic variants results from the non-uniform internal stress due to material inhomogeneities. It should be noted that the modified Landau free energy function is employed to explain the martensite reorientation on the macroscale and the local switching thresholds are regarded to be uniform throughout the specimen. However, the local switching patterns are not identical when the internal stress is considered together with the external loads. That is, the non-uniform internal stress leads to different local switching responses. The effect of internal stress is equivalent to modifying the local switching thresholds. Instead of locally addressing the internal stress, it is reasonable to assume that the local switching thresholds differ and follow a certain distribution property throughout the specimen, and the macroscopic evolution of ξ is regarded as the weighted sum of local switching responses. The evolution between $\xi = 0$ and $\xi = 1$ is homogenized by summing the local switching patterns that count on the values of ϕ . Thus, taking the distribution property into account gives the constitutive relation between ξ and π_ξ by

$$\xi = \begin{cases} \bar{L}_+[\pi_\xi], & \text{for } \dot{\xi} > 0 \\ \bar{L}_-[\pi_\xi], & \text{for } \dot{\xi} < 0 \end{cases} \quad (21)$$

where $\bar{L}_+[\cdot]$ and $\bar{L}_-[\cdot]$ denote the homogenized switching patterns, given by

$$\bar{L}_+[u] = \int_0^{\phi_{\max}} \lambda(\phi) L_\phi^+[u] d\phi, \quad (22)$$

and

$$\bar{L}_-[u] = \int_0^{\phi_{\max}} \lambda(\phi) L_\phi^-[u] d\phi \quad (23)$$

Here, ϕ_{\max} denotes the maximum local threshold for martensitic switching in the material and $\lambda(\phi)$ is the corresponding density function for different local thresholds. The integrals in Eqs. (22, 23) can be discretized and computed using Gaussian quadrature. It is evident that the homogenization yields the smooth evolution of ξ that enables the martensitic variant reorientation to develop gradually. Combined with Eqs. (11, 12, 13, 14), the improved evolution rule for ξ , i.e., Equation (21), can simulate the strain and magnetization responses for arbitrary 2D magneto-mechanical loadings.

Nonetheless, the current model is still incompetent to tackle the partial reorientations with satisfactory accuracy, which are commonly reported in the measurements of magnetic-field-induced-strain. To improve the modeling accuracy and efficiency, the concept of density reassignment [31] is resorted to predict the evolution of ξ for incomplete reorientations in this section. Figure 3a provides the non-overlapping ascending and descending paths for ξ , in which the martensitic variants will completely reorient to each other if the force varies between π_ξ^A and π_ξ^B . The volume fraction ξ^A is equal to zero, indicating that the specimen is fully occupied by V_2 . If the point A is selected as the initial state and the force increases from π_ξ^A to π_ξ^B , the reorientation from V_2 to V_1 will start and V_1 will grow at the expense of V_2 until V_2

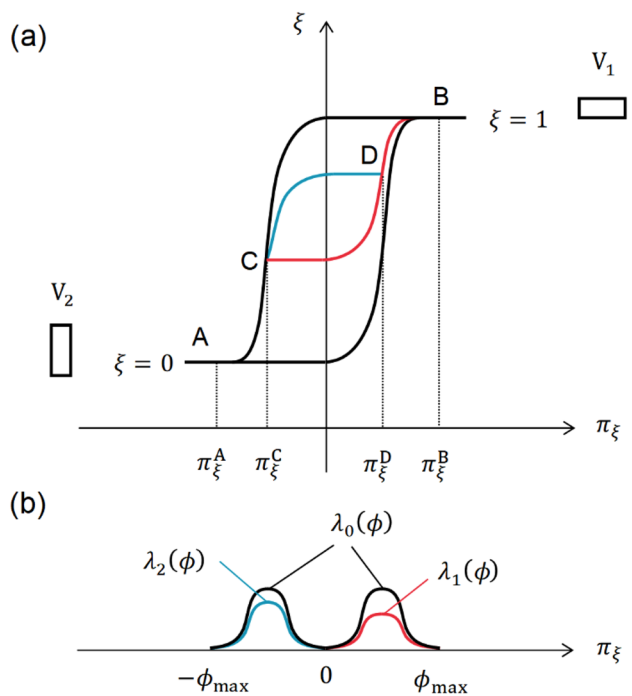


Fig. 3 **a** An illustration of partial martensite reorientations with the corresponding reversal curves, and **b** the concept of density reassignment

vanishes at the point B, indicating that $\xi^B = 1$. The reorientation from V_1 to V_2 will start as the force is lowered and the initial state of $\xi^A = 0$ is restored when the force reaches π_ξ^A again. As shown in Fig. 3b, the density function of local thresholds is designated as $\lambda_0(\phi)$, which is associated with complete reorientation.

The specimen will undergo incomplete martensite reorientation when the specimen is partially loaded. As illustrated in Fig. 3a, the descending of ξ is interrupted and the loading direction is reversed at the intermediate point C. The forward reorientation, i.e. from V_1 to V_2 , has not finished yet when the force decreases to π_ξ^C . The evolution of ξ is unsaturated, i.e., $0 < \xi^C < 1$, resulting in a mixed configuration of V_1 and V_2 at the reversal point. The reverse reorientation, i.e., from V_2 to V_1 , initiates as the force increases from π_ξ^C . It is assumed that the coexistence of V_1 and V_2 affects the internal stress field and thus the distribution of local switching thresholds. That is, the local thresholds are redistributed over the subsequent reverse reorientation. The first-order reversal curve CB is then constructed with a reassigned density function $\lambda_1(\phi)$. In this paper, the reassigned density function takes the simplest form

$$\lambda_1(\phi) = \eta_1 \lambda_0(\phi), \quad (24)$$

where η_1 is the scaling factor that depends on the loading history. The partial forward reorientation starts from the point B and ends at the point C in Fig. 3a. After the reversal, the remnant V_1 is undisturbed and the first-order reversal curve CB reflects the reverse reorientation from V_2 to V_1 . Since the volume fraction of V_2 is $1 - \xi^C$ at the reversal point, it is intuitive to choose the scaling factor as.

$$\eta_1 = 1 - \xi^C \quad (25)$$

The first-order reversal curve CB is then derived with the redistributed density function $\lambda_1(\phi)$ plotted in Fig. 3b. The utilization of the reassigned density function is equivalent to estimating the reversal curve CB by scaling the branch AB with a factor of η_1 . It is evident that the scaling factor η_1 is related to the material configuration at the reversal point and the initial state. Moreover, the choice of η_1 guarantees the continuity of evolving paths at the points B and C. Similar manipulation can be extended for higher-order reversal curves and internal loops with necessary information of loading history. For illustration, the second-order reversal curve DC is formed if the loading direction is reversed at the point D. The reassigned density function is expressed as

$$\lambda_2(\phi) = \eta_2 \lambda_0(\phi), \quad (26)$$

and the scaling factor η_2 is given by

$$\eta_2 = \frac{\xi^D - \xi^C}{1 - \xi^C}, \quad (27)$$

which guarantees the continuity of evolving paths at the points C and D. With the concept of density reassignment, the reversal curves are obtained by scaling the ascending and descending branches for complete reorientations, which facilitates the prediction of incomplete reorientations. The strategy of density reassignment mainly comes from the self-similarity between the interior reversal curves and the exterior switching branches. However, it should be noted that the strategy not only comes from the geometrical consideration, but also takes the physical aspects of prediction into account. The proposed strategy relies on the assumption of distributed local thresholds for martensite reorientation in the sample. For incomplete reorientations, the distribution for the thresholds are modified by the scaling factor. The idea of scaling combines the geometrical and physical insights and makes the prediction easily implemented with accuracy and efficiency.

4 Numerical validation

As mentioned earlier, five state variables are used to quantify microscopic mechanisms under 2D external loads. These state variables can be updated by numerically solving the governing equations, and the strain and magnetization responses are determined from the evolution of state variables. The most commonly used loading condition for Ni–Mn–Ga samples is illustrated in Fig. 4, where the uniaxial stress is applied in the axial direction and the magnetic field is applied in the

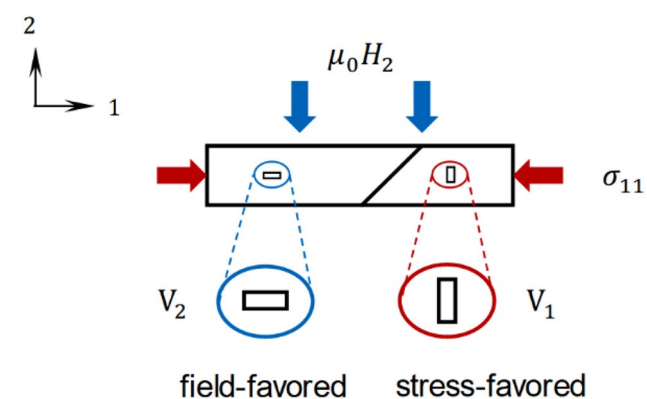


Fig. 4 The most widely used loading condition is when the stress is applied in the 1-direction and the magnetic field is applied in the 2-direction

transverse direction. Considering the preferences for martensitic variants under different types of external loads, V_1 and V_2 are also referred to as the stress-favored variant and the field-favored variant in the following discussion. Since the direction of the external field is perpendicular to the magnetic easy axis of V_2 but parallel to that of V_1 , it is believed that the applied field does not affect the magnetic domain wall motion inside V_1 or the rotation of the magnetization vector inside V_2 . That is,

$$\alpha_1 = 1/2, \quad \text{and} \quad \theta_2 = 0 \quad (28)$$

are expected to hold during both loading and unloading paths, which are used to derive the reduced evolution rules for θ_1 and α_2 . Plugging Eq. (28) into Eq. (13) gives the explicit solution for θ_1 as

$$\sin\theta_1 = \begin{cases} \frac{H_2}{D_2 M_s} - (1-\xi)(2\alpha_2 - 1), & \text{if } \left| \frac{H_2}{D_2 M_s} - (1-\xi)(2\alpha_2 - 1) \right| < \frac{2K_u}{\mu_0 D_2 M_s^2} + \xi \\ \frac{2K_u}{\mu_0 D_2 M_s^2} + \xi, & \text{otherwise} \\ \text{sgn}(H_2), & \text{otherwise} \end{cases} \quad (29)$$

Besides, it is presumed that the domain wall motion in V_2 is dominated by the rotation of θ_2 and the change of θ_1 has a minor effect on the evolution of α_2 [15]. Thus, the first term in Eq. (12) vanishes and the evolution rule for α_2 is further reduced to

$$\alpha_2 = \begin{cases} \frac{1}{2} + \frac{H_2}{2(1-\xi)D_2 M_s}, & \text{if } |H_2| < (1-\xi)D_2 M_s \\ \frac{1}{2} + \frac{1}{2}\text{sgn}(H_2), & \text{otherwise} \end{cases} \quad (30)$$

The driving force for martensite reorientation is also reduced to

$$\begin{aligned} \pi_\xi(\sigma_{11}, H_2, \alpha_i, \theta_i, \xi) &= \frac{\sigma_{11}^2}{2} \left(\frac{1}{E_1} - \frac{1}{E_2} \right) \\ &- \sigma_{11}\epsilon_r - K_u \sin^2 \theta_1 - \mu_0 D_2 M_s^2 (\sin \theta_1 - (2\alpha_2 - 1)) \\ &\left(\xi \sin \theta_1 + (1-\xi)(2\alpha_2 - 1) - \frac{H_2}{D_2 M_s} \right), \end{aligned} \quad (31)$$

where E_1 and E_2 denote Young's moduli for V_1 and V_2 . The evolution of ξ is then solved with the MATLAB function fsolve by substituting the reduced driving force into the constitutive relation, i.e., Equation (21). Herein, the normal density function is chosen to manifest the distribution property of local thresholds and obtain the homogenized evolution rule for complete reorientations. The mean value and standard deviation for the normal distribution are given by $\phi_{\max}/2$ and $\phi_{\max}/6$, respectively. It is worth noting that the property of normal distribution is assumed

for the sake of simplicity, and the density function $\lambda(\phi)$ can be modified to improve the modeling accuracy.

Besides, the temperature dependences of the proposed model need to be addressed. It is worth noting that the temperature is incorporated in the current model from two aspects. On the one hand, some material properties vary with the temperature T , and their temperature dependences are determined from curve fitting. The saturation magnetization M_s and the anisotropy constant K_u decrease with the increasing temperatures, which are fitted by the powers of cosine functions [33]. That is,

$$M_s(T) = M_0 \cos^p \left(\frac{\pi T}{2T_c} \right), \quad (32)$$

and

$$K_u(T) = K_0 \cos^q \left(\frac{\pi T}{2T_c} \right), \quad (33)$$

where T_c denotes the Curie temperature of the Ni–Mn–Ga sample, and M_0 , p , K_0 and q are material constants to be identified from standard tests for magnetic properties at different temperatures. Like the magnetic properties, the martensite tetragonality is also found to decline when the material temperature rises, whose temperature dependence can be characterized by a similar form, i.e.

$$\epsilon_r(T) = k_\epsilon \cos^r \left(\frac{\pi T}{2T_0} \right) + \epsilon_0, \quad (34)$$

where T_0 refers to the austenite transformation temperature, and k_ϵ , r , and ϵ_0 are the material constants that need to be determined from the measured values at different temperatures. As demonstrated in Fig. 18b, c, Eqs. (32, 33, 34) effectively capture these temperature-dependent properties of the Ni–Mn–Ga sample. On the other hand, the constitutive relation between ξ and π_ξ is temperature-dependent as well. It is reported in [25, 26] that the twinning stress increases as the material temperature decreases. Thus, it is reasonable to assume that the material temperature affects the internal stress distribution, and thereby, the maximum switching threshold ϕ_{\max} . Specifically, the maximum threshold is presumed to vary linearly with the material temperature, given by

$$\phi_{\max}(T) = k_\phi T + \phi_0, \quad (35)$$

where k_ϕ and ϕ_0 are the model parameters to be identified. It should be clarified that the linear dependence is adopted for simplicity. One can use nonlinear functions to estimate the temperature dependence of ϕ_{\max} as well.

Table 1 The material constants and model parameters used in the numerical examples

Description	Value	Unit	Description	Value	Unit
ρ	8.02×10^3	$\text{kg} \cdot \text{m}^{-3}$	k_e	-2.80×10^{-2}	—
E_1	5.37×10^3	MPa	r	0.536	—
E_2	1.77×10^3	MPa	ε_0	4.86×10^{-2}	—
T_c	373	K	D_1	0.216	—
M_0	7.04×10^5	$\text{A} \cdot \text{m}^{-1}$	D_2	0.392	—
p	0.205	—	κ_1	3.55	MPa
K_0	3.15×10^5	$\text{J} \cdot \text{m}^{-3}$	k_ϕ	-1.62×10^{-3}	$\text{MPa} \cdot \text{K}^{-1}$
q	0.585	—	ϕ_0	0.598	MPa
T_0	315	K	—	—	—

5 Results and discussion

In this section, the proposed model is numerically implemented in MATLAB and the model predictions are compared with the experimental data in [8, 26] as well as with the simulation results in [18, 21] to demonstrate the magneto-mechanical coupling nature and validate the temperature dependences of the current model. The material constants and the model parameters used in the numerical examples are given in Table 1, and the details of the model calibration are summarized in the Appendix.

Figures 5, 6, and 7 present the strain and magnetization responses for field-assisted super-elasticity under room temperature, i.e., $T = 293\text{K}$. In the experiment, a sufficiently high magnetic field was first applied in the 2-direction to ensure that the sample is full of the field-favored variants, indicating that the sample is at its maximum length in the 1-direction. The external field was then decreased to the

desired test level and kept constant afterward. Varying stress between 0 and 10MPa was loaded in the 1-direction to drive the reorientation from the field-favored variants to the stress-favored variant. In Figs. 5, 6, and 7, the constant bias magnetic fields are $\mu_0 H_2 = 0$, $\mu_0 H_2 = 0.4\text{T}$, and $\mu_0 H_2 = 1.1\text{T}$. The model predictions agree well with the experimental results under different levels of bias magnetic field. It is worth noting that the root-mean-square (RMS) errors between the predicted results and the measured ones are utilized to evaluate the model accuracy. The RMS strain errors are 2.36×10^{-3} , 5.26×10^{-3} , and 4.47×10^{-3} , while the RMS errors for the relative magnetization are 0, 1.33×10^{-1} , and 0. Besides, the field dependences on the stress-induced martensitic variant reorientation are also successfully captured. The numerical simulation is carried out for different levels of constant magnetic field, and the field dependences of the reversible strain and the switching stress are illustrated in Fig. 8, where the switching stress σ_{tw} is defined as the applied stress inducing 1% strain during the loading path

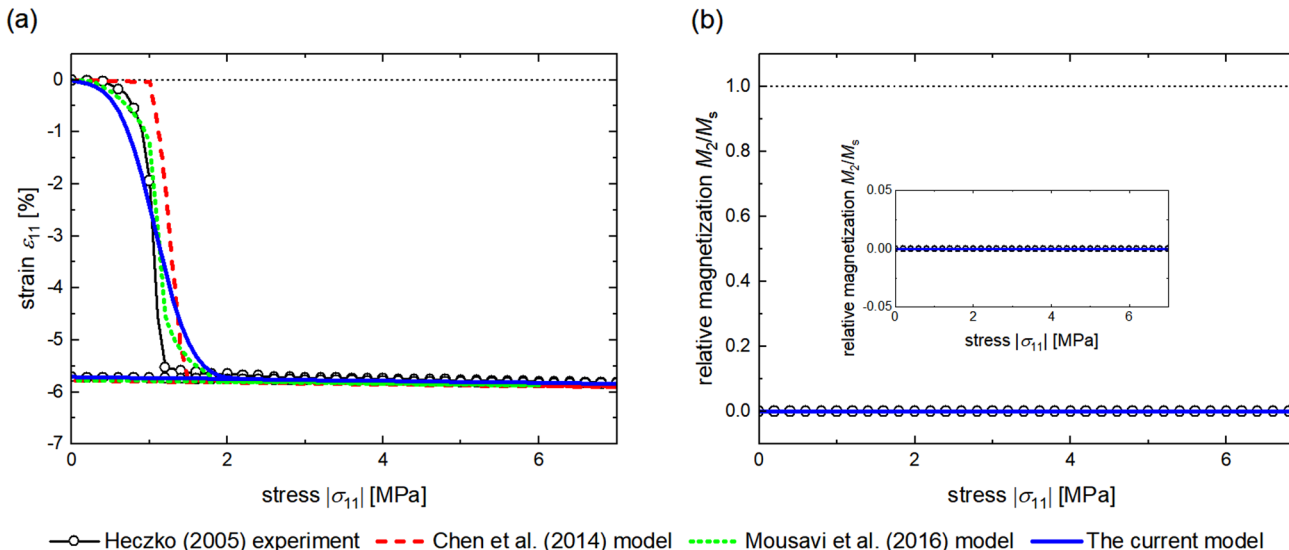


Fig. 5 Comparisons between the model predictions and the experimental data in [8] as well as the simulation results in [18, 21] for the field-assisted super-elasticity under $\mu_0 H_2 = 0$ at $T = 293\text{K}$: **a** strain, and **b** relative magnetization

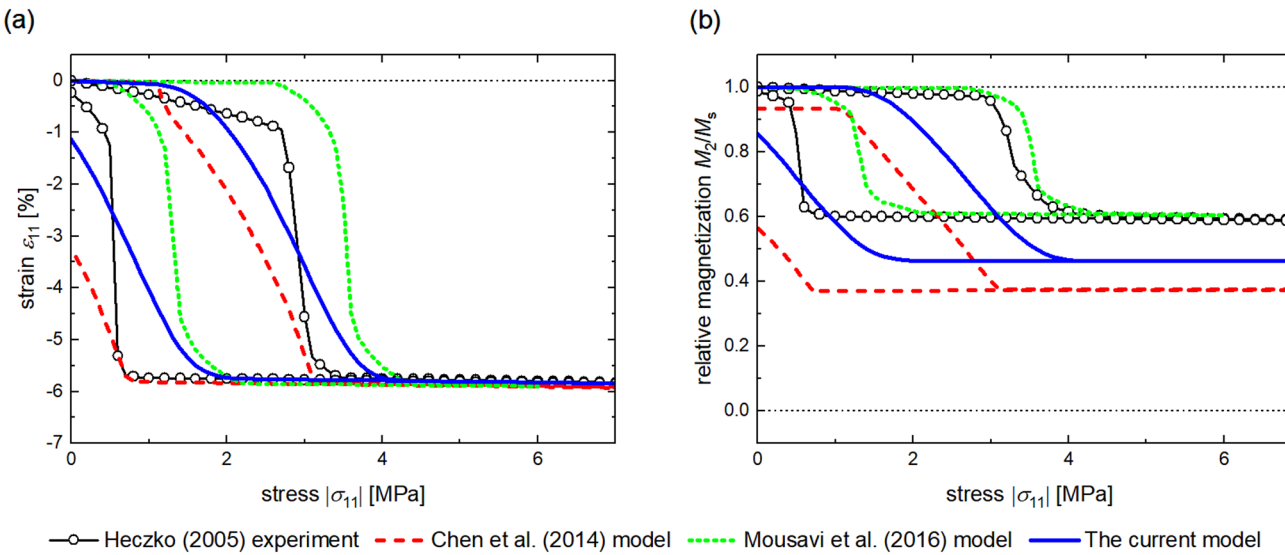


Fig. 6 Comparisons between the model predictions and the experimental data in [8] as well as the simulation results in [18, 21] for the field-assisted super-elasticity under $\mu_0 H_2 = 0.4\text{T}$ at $T = 293\text{K}$: **a** strain, and **b** relative magnetization

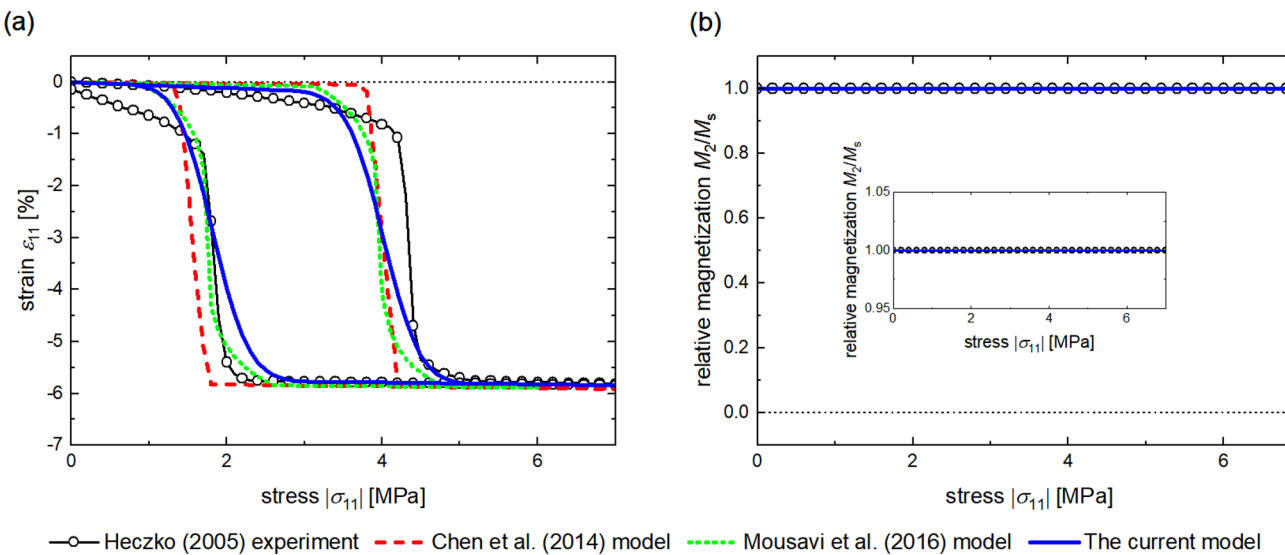


Fig. 7 Comparisons between the model predictions and the experimental data in [8] as well as the simulation results in [18, 21] for the field-assisted super-elasticity under $\mu_0 H_2 = 1.1\text{T}$ at $T = 293\text{K}$: **a** strain, and **b** relative magnetization

to indicate the onset of martensite reorientation. As can be observed, the higher the magnetic field level, the higher the compressive stress needed to activate the reorientation from V_2 and V_1 . For the super-elastic tests, the bias magnetic field is applied to restore the sample to the field-favored variant configuration when the stress is unloaded. Therefore, the reversible strain naturally increases with the increasing level of bias magnetic field. For the field-free uniaxial compression test, i.e., $\mu_0 H_2 = 0$, the unloading of the compressive stress is insufficient to induce the reverse reorientation. The deformation is nearly irreversible and a giant residual strain

is found at the end of the stress cycle. In contrast to the giant residual strain, no magnetization response is detected for the field-free test. The initial field-favored configuration is completely recovered at a high magnetic field, i.e., $\mu_0 H_2 = 1.1\text{T}$, as the compressive stress is unloaded. Even though the strain varies with the applied stress, the magnetization remains saturated during the entire cycle. At the intermediate magnetic field, i.e., $\mu_0 H_2 = 0.4\text{T}$, only partial recovery of the field-favored variant is observed, and the magnetization changes with the external stress within a certain range.

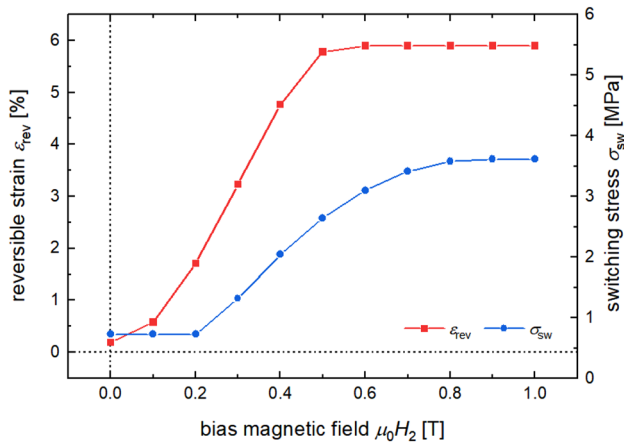


Fig. 8 Model predictions on the field dependences of reversible strain and switching stress for the field-assisted super-elastic effect at room temperature

Figures 9, 10, 11 illustrate the measurements and predictions for strain and magnetization responses with respect to the magnetic shape memory effect under $T = 293\text{K}$. According to the experimental procedure, the sample was first compressed by high-level stress in the 1-direction such that the field-favored variant is eliminated. That is, the sample is of the stress-favored variant state and at its minimum length in the 1-direction. The stress is then lowered to the desired test level, and kept constant for the remainder of the experiment. The application of a varying magnetic field between -1.15T and 1.15T in the 2-direction leads to the reorientation from the stress-favored variant to the field-favored variant. The stress levels are $\sigma_{11} = -0.6\text{MPa}$, $\sigma_{11} = -1.4\text{MPa}$, and

$\sigma_{11} = -3.0\text{MPa}$ in Figs. 9, 10, and 11. Good agreements between the model predictions and the experiment measurements indicate the model capability and its adaptability in magneto-mechanical coupling. The RMS strain errors are 6.08×10^{-3} , 6.78×10^{-3} , and 8.85×10^{-4} , while the RMS errors in the relative magnetization plots are 7.28×10^{-2} , 7.76×10^{-2} , and 2.77×10^{-2} . It is noticeable that the field-induced martensite variant reorientation depends on the applied stress level, and the proposed model can quantitatively simulate this stress-dependent behavior. The proposed model is implemented for different bias stress levels and the stress dependences of the switching field and the maximum and reversible strain are given in Fig. 12, where the switching field $\mu_0 H_{\text{sw}}$ denotes the applied magnetic field inducing 1% strain in the first magnetizing cycle. As is presented, the higher the stress level, the higher the magnetic field needed to start the reorientation. The maximum strain decreases with the increasing bias stress. As seen in Fig. 11, the field-induced reorientation is absolutely suppressed and no magnetic-field-induced strain is measured when high-level bias stress is applied. It is observed that the stress-favored configuration is always partially restored under low stress levels. Since the role of the compressive stress is to recover the sample to the initial stress-favored state, the reversible strain initially increases with the bias stress. The stress-favored configuration is completely restored when the bias stress reaches a certain level. That is, the magnetic-field-induced strain is completely reversible after the bias stress reaches this level. The reversible strain achieves its maximum at this stress level and decreases with further increasing bias stress. In addition to the strain behavior, the magnetization responses exhibit stress dependences as well. A tilt occurs

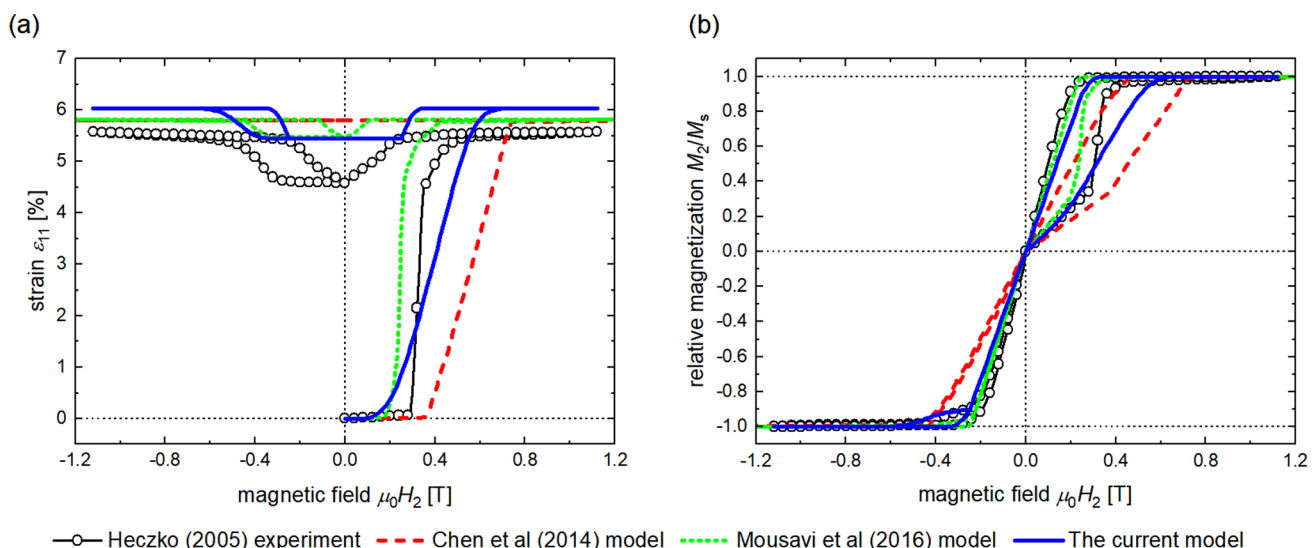


Fig. 9 Comparisons between the model predictions and the experimental data in [8] as well as the simulation results in [18, 21] for the magnetic shape memory effect under $\sigma_{11} = -0.6\text{MPa}$ at $T = 293\text{K}$: **a** strain, and **b** relative magnetization

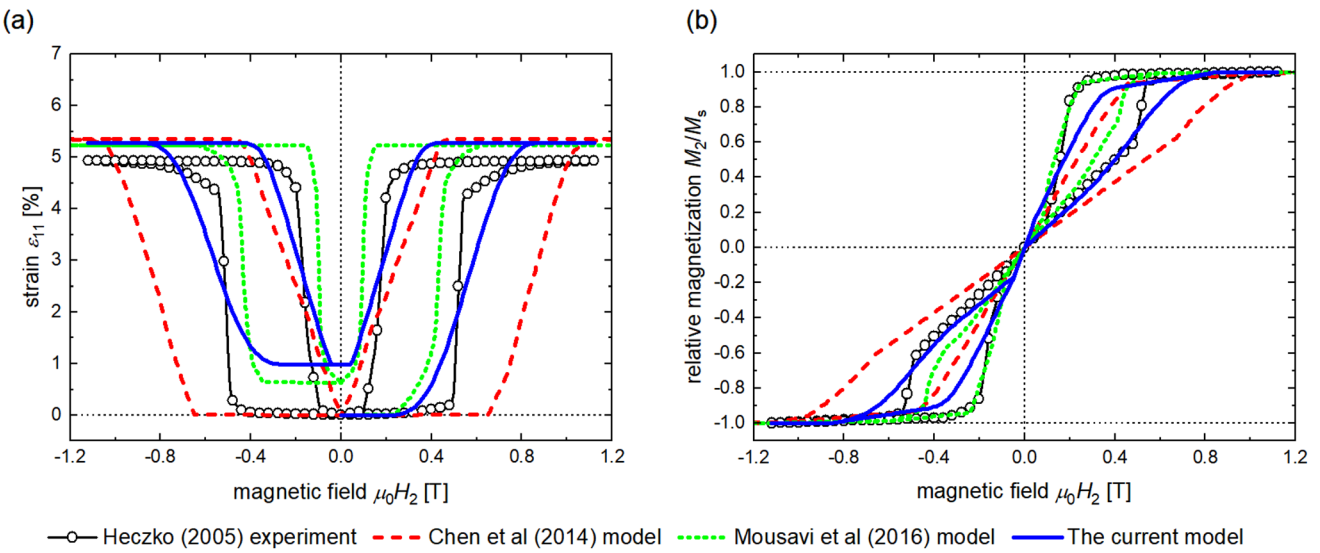


Fig. 10 Comparisons between the model predictions and the experiment data in [8] as well as the simulation results in [18, 21] for the magnetic shape memory effect under $\sigma_{11} = -1.4\text{MPa}$ at $T = 293\text{K}$: **a** strain, and **b** relative magnetization

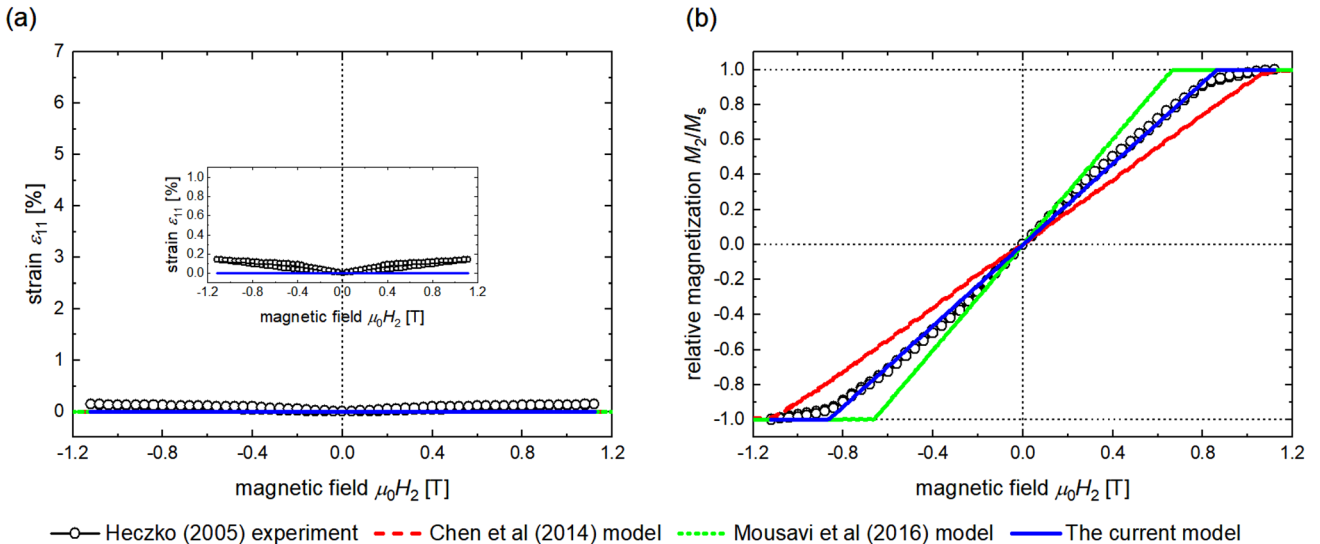


Fig. 11 Comparisons between the model predictions and the experimental data in [8] as well as the simulation results in [18, 21] for the magnetic shape memory effect under $\sigma_{11} = -3.0\text{MPa}$ at $T = 293\text{K}$: **a** strain, and **b** relative magnetization

in the magnetization response when the martensite reorientation starts around the switching field. Despite the applied stress levels being different, unlike the induced strain, it is reported that the magnetization is always saturated at a sufficiently high magnetic field. It is obvious that the magnetic-field level for saturation increases with the increasing bias stress.

Figures 13, 14, and 15 give the quantitative representation of the temperature dependences on the magnetic shape memory effect, in which the corresponding tests were carried out with the bias stress level of $\sigma_{11} = -1.0\text{MPa}$

under $T = 228\text{K}$, $T = 288\text{K}$, and $T = 307\text{K}$, respectively. Since the testing procedure for the magnetic shape memory effect has been discussed above, there is no need to repeat it. In Figs. 13, 14, and 15, the proposed model basically captures the trends in the strain and magnetization responses for tests under three temperatures. The RMS strain errors are 6.71×10^{-3} , 1.04×10^{-2} , and 8.22×10^{-3} , while the RMS errors for the relative magnetization are 7.00×10^{-2} , 1.00×10^{-1} , and 6.44×10^{-2} . As demonstrated in Fig. 16, the model predictions are compared with the measured data to validate the temperature dependences

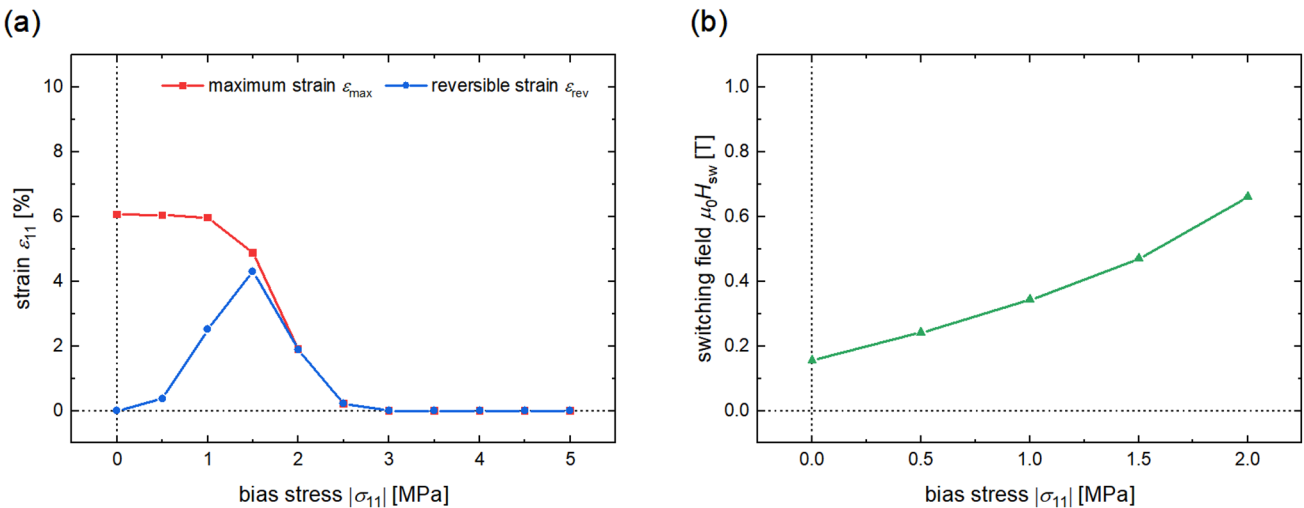


Fig. 12 Model predictions on the stress dependences of **a** maximum and reversible strain, and **b** switching field for the magnetic shape memory effect

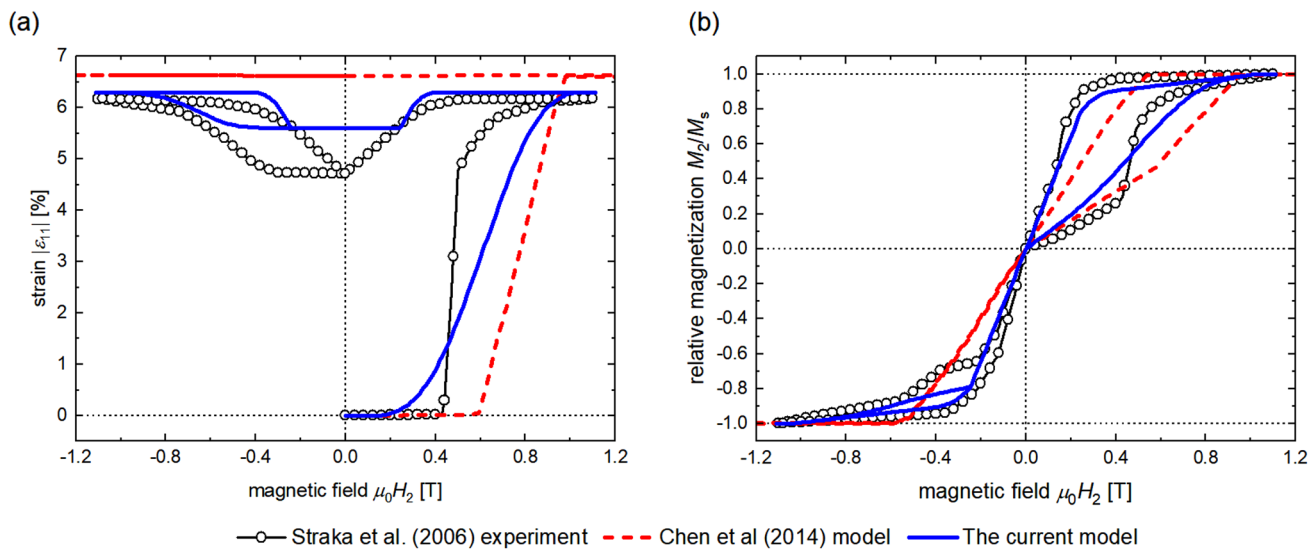


Fig. 13 Comparisons between the model predictions and the experimental data in [26] as well as the simulation results in [18] for the magnetic shape memory effect under $\sigma_{11} = -1.0 \text{ MPa}$ at $T = 223 \text{ K}$: **a** strain, and **b** relative magnetization

of the current framework. It is accurately captured by the proposed model that the magnetic field needed for the onset of the reorientation, namely the switching field, decreases with the increasing temperature. The maximum strain decreases while the reversible strain increases as the material temperature rises. Moreover, the twinning stress σ_{tw} is computed for several material temperatures that is the stress needed to induce 3% strain in the field-free compression test. The simulated results are plotted with the measured ones in Fig. 17 to further demonstrate the modeling accuracy. It is worth noting that the temperature dependences of the current model come from the

temperature-dependent correlation between the generalized driving force and the constitutive relation for martensite reorientation. For one thing, the maximum local threshold ϕ_{\max} for reorientation is assumed to vary linearly with the material temperature, modifying the constitutive law between ξ and π_ξ under different temperatures. For another, the material constants i.e., ε_r , K_u and M_s , vary with the material temperature. Even if the tests are carried out under the same magneto-mechanical conditions, the temperature-varying material constants result in different driving forces π_ξ at different temperatures. In the current paper, the local thresholds are presumed to be normally

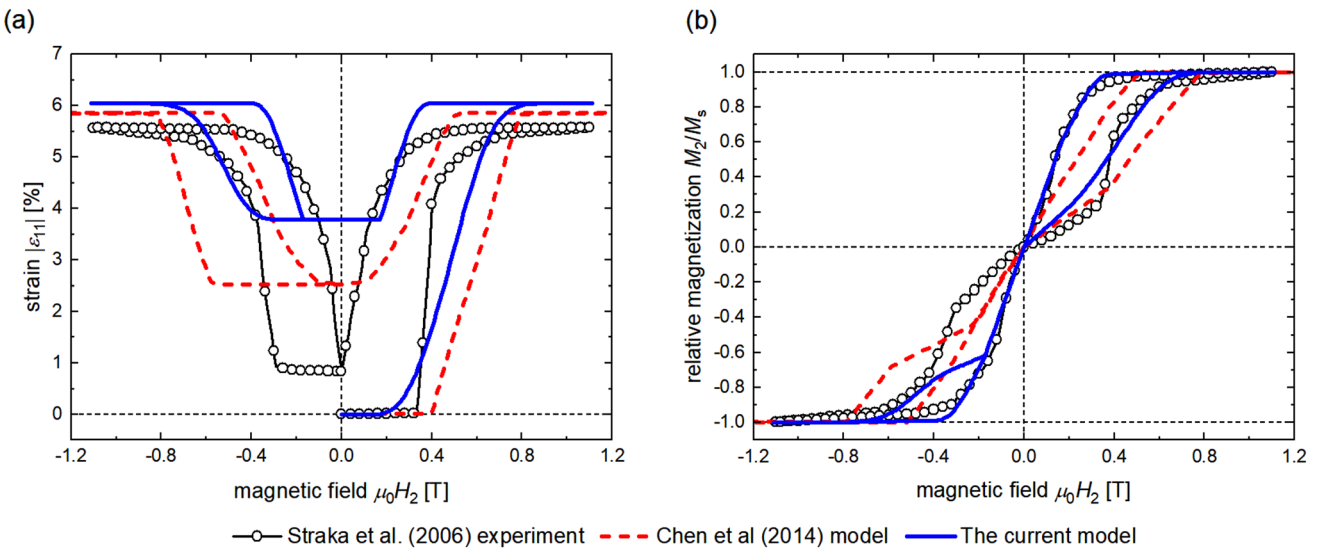


Fig. 14 Comparisons between the model predictions and the experimental data in [26] as well as the simulation results in [18] for the magnetic shape memory effect under $\sigma_{11} = -1.0\text{MPa}$ at $T = 288\text{K}$: **a** strain, and **b** relative

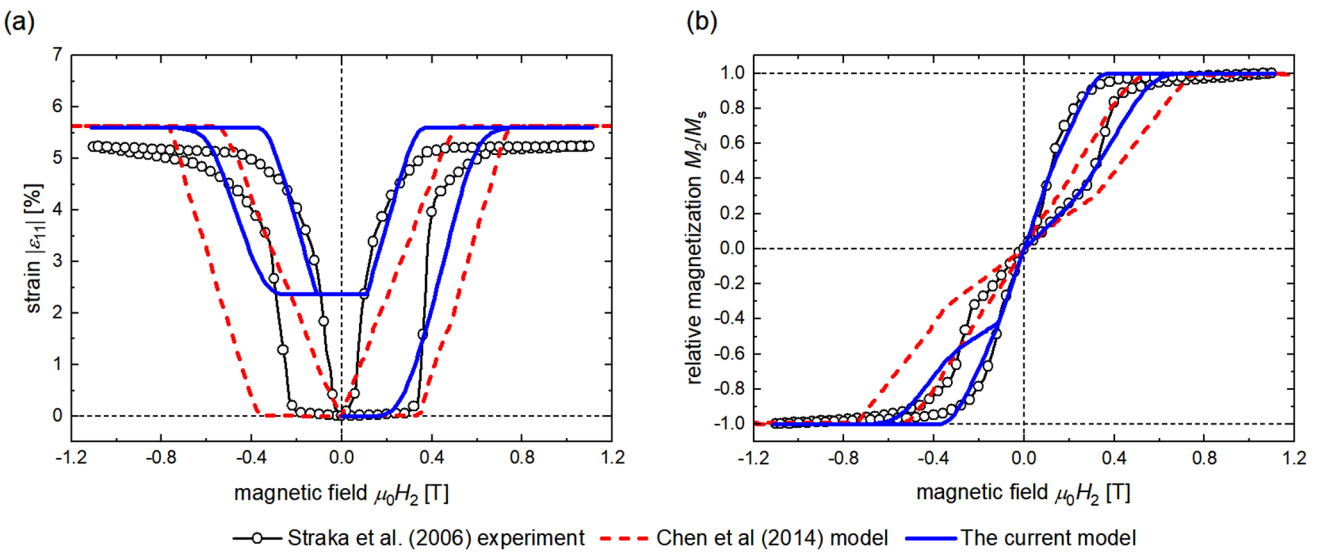


Fig. 15 Comparisons between the model predictions and the experimental data in [26] as well as the simulation results in [18] for the magnetic shape memory effect under $\sigma_{11} = -1.0\text{MPa}$ at $T = 307\text{K}$: **a** strain, and **b** relative magnetization

distributed, the temperature dependence of this property is simply delineated by the linear variation of ϕ_{\max} . Thus, one possible way to improve the prediction accuracy and flexibility is to introduce another temperature-varying parameters to address the temperature dependences of local thresholds distribution.

The proposed model correlates the evolution of state variables to the strain and magnetization responses, and the energy relations are carefully formulated to characterize the coupled magneto-mechanical behavior. The assumption of local switching thresholds and the concept

of density reassignment are developed, making the current model superior in its modeling accuracy and adaptability. The temperature dependences of the material constants and the model parameters are also addressed to simulate the material responses under different temperatures. In this work, the model predictions exhibit good agreement with the experimental data. Even though the predicted results are satisfactory compared to the previous models, the improvement in modeling accuracy is not shown in several plots. This can be explained by the differences between the models. The previous models [18, 21] are developed within the

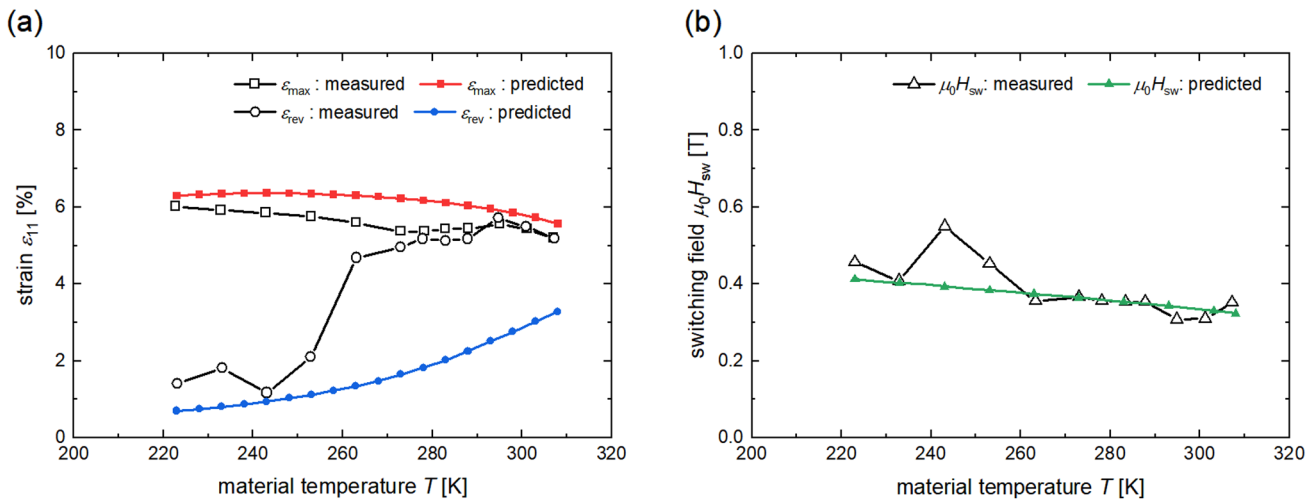


Fig. 16 Comparisons between the model predictions and the experimental data in [26] on the temperature dependences of **a** maximum and reversible strain, and **b** switching field for the magnetic shape memory effect

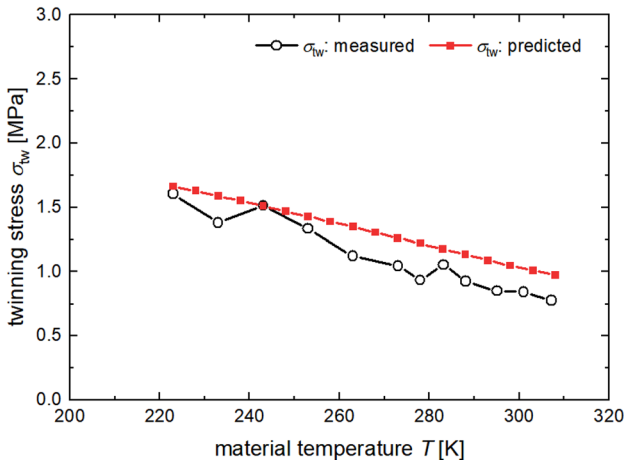


Fig. 17 Comparisons between the model predictions and the experimental data in [26] on the temperature dependences of the twinning stress

thermodynamic framework of irreversible processes. The physical aspects of the simulation are emphasized in their works, where all three martensitic variants are considered and the reorientation process is simulated by plastic hardening. Unlike these models, the presented model utilizes a different strategy to investigate martensite reorientation. Martensite reorientation is delineated by the hysteretic switching between stable equilibria, and only two variants are taken into account for convenience. It is worth noting that the presented model compromises some physical considerations to reduce the model complexity, resulting in a limited improvement in modeling accuracy compared to previous simulation

results. The discrepancies between the model predictions and the experiment data mainly come from two aspects. For one thing, the discrepancies come from the modified Landau free energy function which is defined by piecewise quadratic polynomials. The quadratic function further leads to the piecewise linear switching that is governed by two coefficients. Even if the linear form would capture the hysteresis behavior, the linearity restricts the flexibility of the proposed model. For another, the assumption of normally distributed local thresholds compromises the modeling accuracy as well. As mentioned earlier, the normal density function is employed for simplicity, and the corresponding coefficients are determined by the parameter ϕ_{\max} . Such a distribution property can not precisely capture all the characteristics shown in the measurement. In practice, some improvements can be made to effectively diminish the prediction error. Generally, the prediction errors for the macroscopic responses can be reduced if more experimental data are exploited to validate the proposed model. One possible way to improve the modeling accuracy is to modify the form of the double-well potential and incorporate nonlinearity into the local switching pattern. The other way is to utilize other types of density functions, or directly estimate the discrete densities by curve fitting. New model parameters will be introduced in both ways, which will complicate the model and enhance its flexibility. Besides, the temperature dependences of these extra parameters must be carefully resolved from experimental observations to capture the trends of strain and magnetization responses at different temperatures, and thus reduce the prediction errors.

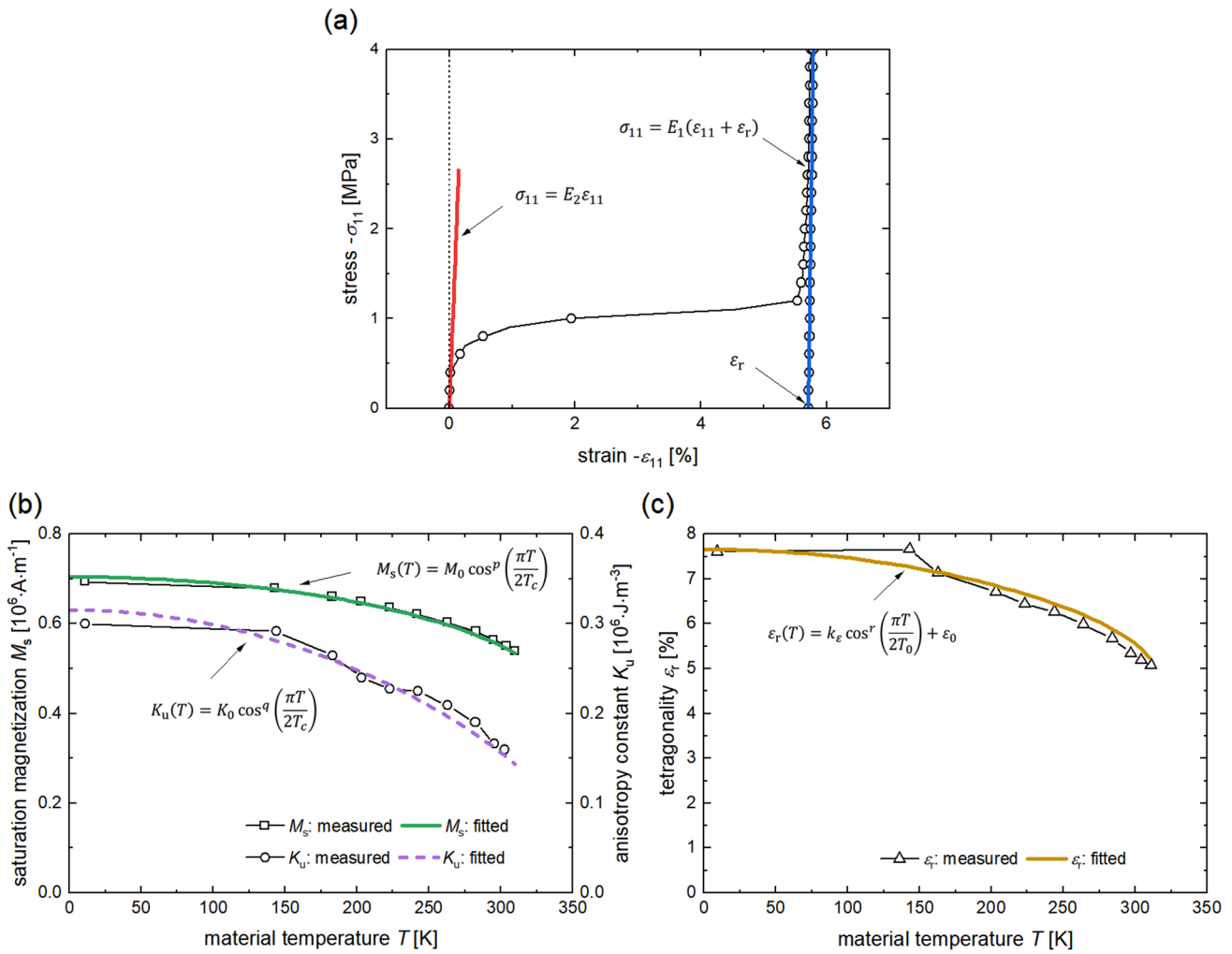


Fig. 18 Calibration of several material constants: **a** Young's moduli fitted from the measured stress-strain data in [8], **b** temperature-dependent magnetic properties fitted using the reported data in [25],

and **c** temperature-dependent martensite tetragonality fitted using the reported data in [25]

6 Conclusion

In this work, a phenomenological model has been presented to study the macroscopic responses under 2D magneto-mechanical loadings. Targeted to simulate the magneto-mechanical behavior, the proposed model utilizes five state variables to account for three competing microscopic mechanisms. The evolution rules for these state variables are phenomenologically found from the minimum energy principle. The modified Landau free energy function is involved in the energy formulation, and the hysteresis unit is formulated to characterize the switching between the martensitic variants. The constitutive law for martensite reorientation is upgraded with the assumption of the distributed thresholds for local switching, and the normal density function is chosen to characterize the distribution property. The concept of density

reassignment is deployed to predict the reversal curves for incomplete reorientation. To validate the model capability, the model formulation has been numerically implemented for the most widely used loading condition in which the uniaxial stress and the magnetic field are applied perpendicular to each other. Besides, the temperature-dependent material constants and model parameters are discussed to characterize the temperature dependences of martensitic variant reorientation. The model predictions have been compared with the experiment results and the previous simulation ones. Good agreements between the modeling results and the experimental counterparts demonstrate the effectiveness and adaptability of the presented model. It is worth noting that the proposed model successfully captures the magneto-mechanical couplings and predicts the temperature-dependent strain and magnetization responses. In addition to the

model accuracy, simple formulation and low computational cost provide the current model with the potential to facilitate the design and control of the FSMA-based smart structures.

Appendix

Model calibration

In this work, the experimental data in [8, 26] are employed to validate the model capabilities, in which the single crystalline Ni_{49.7}Mn_{29.1}Ga_{21.2} (at %) rectangular prism 9 × 5 × 5 mm³ in size was used for the simultaneous measurement of the strain and magnetization responses. Besides, several reported data in [25] are employed to characterize the temperature-dependent properties of the Ni–Mn–Ga sample. The model calibration is discussed in this section, providing the details on the identification of the material constants and the model parameters given in Table 1.

The Curie temperature T_c , and the austenitic transformation temperature T_0 are taken from [25], while the mass density ρ are taken from [34]. Other material constants are determined from the experimental data by curve fitting. As shown in Fig. 18a, Young's moduli E_1 and E_2 can be obtained using the stress–strain data under zero bias field in [8]. The reported data in [25] are exploited to illustrate the temperature dependences of the magnetic properties and the martensite tetragonality in Fig. 18b, c, from which the constants M_0 , p , K_0 , q , k_ϵ , r , and ϵ_0 are fitted. Apart from these material constants, there are several model parameters to be identified in the proposed model. Given the specimen size, the diagonal entries of the demagnetization tensor, i.e., D_1 and D_2 , can be simply computed using the analytic formula in [35]. In this work, the identification of the remaining parameters, i.e., κ_1 , k_ϕ , and ϕ_0 , is treated as a least-square optimization problem, which is to minimize the error between the modeling results and experimental counterparts. These parameters are utilized to compute the predicted strain and magnetization responses and then updated by optimizing the prediction error. Herein, the optimization problem is given by

$$\min_{\kappa_1, k_\phi, \phi_0} \sum_{j=1}^N \left(\frac{\hat{\epsilon}_j - \epsilon_j}{\epsilon_{\max}} \right)^2 + \left(\frac{\hat{M}_j - M_j}{M_s} \right)^2, \quad (36)$$

where $\hat{\epsilon}_j$ and \hat{M}_j denote the measured values of strain and relative magnetization while ϵ_j and M_j denote the predicted ones, and N is the number of the sampled points. ϵ_{\max} is the maximum strain that is used to obtain the relative strain error. The optimization of the prediction error is carried out using the MATLAB function *fminsearch* which is based on

the Nelder-Mead algorithm, and three parameters are calibrated with the measured data in Figs. 7, 10, and 13.

Acknowledgements This work has been supported by the National Natural Science Foundation of China (Grant No. 51575478 and Grant No. 61571007). R. Melnik acknowledges the support from the NSERC and CRC programs.

Declarations

Conflict of interest The authors have no competing interests to declare that are relevant to the content of this article.

References

1. K. Ullakko, Magnetically controlled shape memory alloys: a new class of actuator materials. *J. Mater. Eng. Perform.* **5**, 405–409 (1996)
2. K. Ullakko, J.K. Huang, C. Kantner, R.C. O'Handley, V.V. Kokorin, Large magnetic-field-induced strains in Ni₂MnGa single crystals. *Appl. Phys. Lett.* **69**, 1966–1968 (1996)
3. S.J. Murray, M. Marioni, S.M. Allen, R.C. O'Handley, T.A. Lograsso, 6% magnetic-field-induced strain by twin-boundary motion in ferromagnetic Ni–Mn–Ga. *Appl. Phys. Lett.* **77**, 886–888 (2000)
4. A.A. Likhachev, K. Ullakko, Magnetic-field-controlled twin boundaries motion and giant magneto-mechanical effects in Ni–Mn–Ga shape memory alloy. *Phys. Lett. A* **275**, 142–151 (2000)
5. D.C. Lagoudas, *Shape memory alloys: modeling and engineering applications* (Springer, Berlin, 2008)
6. R.C. O'Handley, Model for strain and magnetization in magnetic shape-memory alloys. *J. Appl. Phys.* **83**, 3263–3270 (1998)
7. S.J. Murray, R.C. O'Handley, S.M. Allen, Model for discontinuous actuation of ferromagnetic shape memory alloy under stress. *J. Appl. Phys.* **89**, 1295–1301 (2000)
8. O. Heczko, Magnetic shape memory effect and magnetization reversal. *J. Magn. Magn. Mater.* **290–291**, 787–794 (2005)
9. J.Y. Li, Y.F. Ma, Magnetoelastic modeling of magnetization rotation and variant rearrangement in ferromagnetic shape memory alloys. *Mech. Mater.* **40**, 1022–1036 (2008)
10. Q. Peng, J. Huang, M. Chen, Effects of demagnetization on magnetic-field-induced strain and microstructural evolution in Ni–Mn–Ga ferromagnetic shape memory alloy by phase-field simulations. *Mater. Des.* **107**, 361–370 (2016)
11. Q. Peng, Q. Sun, M. Chen, Phase-field simulations of partial pseudoelastic stress-strain behavior and microstructure evolution of Ni–Mn–Ga. *Mater. Sci. Eng., A* **669**, 428–436 (2016)
12. H.H. Wu, A. Pramanick, Y.B. Ke, X.L. Wang, Real-space phase field investigation of evolving magnetic domains and twin structures in a ferromagnetic shape memory alloy. *J. Appl. Phys.* **120**, 183904 (2016)
13. B. Kiefer, D.C. Lagoudas, Magnetic field-induced martensitic variant reorientation in magnetic shape memory alloys. *Phil. Mag.* **85**, 4289–4329 (2005)
14. A.B. Waldauer, H.P. Feigenbaum, C. Ciocanel, N.M. Bruno, Improved thermodynamic model for magnetic shape memory alloys. *Smart Mater. Struct.* **21**, 094015 (2012)
15. D.H. LaMaster, H.P. Feigenbaum, I.D. Nelson, C. Ciocanel, A Full two-dimensional thermodynamic-based model for magnetic shape memory alloys. *J. Appl. Mech.* **81**, 061003 (2014)
16. M. Shirani, M. Kadkhodaei, A geometrical approach to determine reorientation start and continuation conditions in ferromagnetic shape memory alloys considering the effects of loading history. *Smart Mater. Struct.* **23**, 125008 (2014)

17. H. Sayyaadi, M.A.A. Farsangi, Frequency-dependent energy harvesting via magnetic shape memory alloys. *Smart Mater. Struct.* **24**, 115022 (2015)
18. X. Chen, Z. Moumni, Y. He, W. Zhang, A three-dimensional model of magneto-mechanical behaviors of martensite reorientation in ferromagnetic shape memory alloys. *J. Mech. Phys. Solids* **64**, 249–286 (2014)
19. D.H. LaMaster, H.P. Feigenbaum, C. Ciocanel, I.D. Nelson, A full 3D thermodynamic-based model for magnetic shape memory alloys. *J. Intell. Mater. Syst. Struct.* **26**, 663–679 (2014)
20. H.P. Feigenbaum, C. Ciocanel, J.L. Eberle, J.L. Dikes, Experimental characterization and modeling of a three-variant magnetic shape memory alloy. *Smart Mater. Struct.* **25**, 104004 (2016)
21. M.R. Mousavi, J. Arghavani, A three-dimensional constitutive model for magnetic shape memory alloys under magneto-mechanical loadings. *Smart Mater. Struct.* **26**, 015014 (2016)
22. T. Bartel, B. Kiefer, A. Menzel, An energy-relaxation-based framework for the modeling of magnetic shape memory alloys—simulation of three-dimensional effects under homogeneous loading conditions. *Int. J. Solids Struct.* **208–209**, 221–234 (2021)
23. O. Heczko, K. Ullakko, Effect of temperature on magnetic properties of Ni-Mn-Ga magnetic shape memory (MSM) alloys. *IEEE Trans. Magn.* **37**, 2672–2674 (2001)
24. N. Glavatska, G. Mogilny, I. Glavatskiy, V. Gavriljuk, Temperature stability of martensite and magnetic field induced strain in Ni–Mn–Ga. *Scripta Mater.* **46**, 605–610 (2002)
25. O. Heczko, L. Straka, Temperature dependence and temperature limits of magnetic shape memory effect. *J. Appl. Phys.* **94**, 7139–7143 (2003)
26. L. Straka, O. Heczko, S.P. Hannula, Temperature dependence of reversible field-induced strain in Ni–Mn–Ga single crystal. *Scripta Mater.* **54**, 1497–1500 (2006)
27. I. Glavatskyy, N. Glavatska, I. Urubkov, J.U. Hoffman, F. Bourd'arot, Crystal and magnetic structure temperature evolution in Ni–Mn–Ga magnetic shape memory martensite. *Mater. Sci. Eng., A* **481–482**, 298–301 (2008)
28. L. Straka, H. Hänninen, O. Heczko, Temperature dependence of single twin boundary motion in Ni–Mn–Ga martensite. *Appl. Phys. Lett.* **98**, 141902 (2011)
29. S. Zhang, X. Chen, Z. Moumni, Y. He, Thermal effects on high-frequency magnetic-field-induced martensite reorientation in ferromagnetic shape memory alloys: an experimental and theoretical investigation. *Int. J. Plast.* **108**, 1–20 (2018)
30. S. Zhang, G. Qin, Y. He, Ambient effects on the output strain of Ni–Mn–Ga single crystal magnetic shape memory alloy. *J. Alloy. Compd.* **835**, 155159 (2020)
31. Y. Han, H. Du, L. Wang, R. Melnik, A phenomenological model for thermally-induced hysteresis in polycrystalline shape memory alloys with internal loops. *J. Intell. Mater. Syst. Struct.* **33**, 1170–1181 (2021)
32. N.N. Sarawate, M.J. Dapino, Magnetomechanical characterization and unified energy model for the quasistatic behavior of ferromagnetic shape memory Ni–Mn–Ga. *Smart Mater. Struct.* **19**, 035001 (2010)
33. H. Lei, L. Tong, Z. Wang, Effect of temperature on magnetic field-induced response of Ni–Mn–Ga single crystals. *J. Intell. Mater. Syst. Struct.* **26**, 2395–2410 (2014)
34. R. Tickle, R.D. James, Magnetic and magnetomechanical properties of Ni₂MnGa. *J. Magn. Magn. Mater.* **195**, 627–638 (1999)
35. A. Aharoni, Demagnetizing factors for rectangular ferromagnetic prisms. *J. Appl. Phys.* **83**, 3432–3434 (1998)

Publisher's Note Springer Nature remains neutral with regard to jurisdictional claims in published maps and institutional affiliations.

Springer Nature or its licensor (e.g. a society or other partner) holds exclusive rights to this article under a publishing agreement with the author(s) or other rightsholder(s); author self-archiving of the accepted manuscript version of this article is solely governed by the terms of such publishing agreement and applicable law.